USC–SIPI REPORT #235

Shape from Shading with a Gerneralized Reflectance Map Model

by

Kyoung Mu Lee and C.-C. Jay Kuo

June 1993

Signal and Image Processing Institute
UNIVERSITY OF SOUTHERN CALIFORNIA
Department of Electrical Engineering-Systems
3740 McClintock Avenue, Room 404
Los Angeles, CA 90089-2564 U.S.A.

Shape from Shading with A Generalized Reflectance Map Model[*]

Kyoung Mu Lee[†]   and   C.-C. Jay Kuo [†]

June 29, 1993

Abstract

Most conventional SFS (Shape from Shading) algorithms have been developed under three basic assumptions on surface properties and imaging geometry to simplify the problem, namely, a Lambertian surface, a distant point light source and orthographic projection. In this research, we derive a general physics-based reflectance map model which includes diffuse and specular reflection effects, a nearby point light source and perspective projection, and then develop a new direct shape recovery algorithm from shaded images. The basic idea of our solution method is to discretize the image irradiance equation with a finite triangular element surface model, to express the resulting nonlinear system of equations in terms of depth variables only, and to recover the object shape by linearizing the nonlinear equations and minimizing a quadratic cost functional. We perform numerical experiments with one or multiple photometric stereo images to demonstrate the performance of the derived physics-based reflectance map model and the proposed SFS algorithm.

1   Introduction

There has been a considerable amount of interest and effort on shape extraction from image intensities in computer vision research for the last several decades. The brightness of a pixel in an image is generated through an image formation process governed by the optical, physical and geometrical factors including the object shape, the surface reflectance property, and the illumination and sensor characteristics. Thus, to get an accurate reconstructed surface, it is crucial to understand and model the whole complicated imaging process. Most conventional SFS algorithms have been developed under three simple but restrictive assumptions on the image formation model to simplify

1

the problem, namely, the ideal Lambertian surface, a distant point light source and orthographic projection [4], [8], [11], [14], [16], [17], [22], [30], etc. However, these assumptions are not valid in practical environments for the following reasons. First, surface reflection in general contains both the diffuse and the specular components. Second, the light source is often located in a finite distance from the object so that the image brightness depends on the distance between every object point and the light source. Third, images are formed through a pin-hole camera which should be modeled by perspective projection, Since conventional SFS algorithms do not use accurate physical and optical models, apparent distortions of reconstructed surfaces often occur in many real applications.

To make SFS algorithms practically useful, we have to consider a more realistic model of surface reflection and the imaging process. Several attempts to relax the above restrictive assumptions have been made for recent years [2], [7], [10], [13], [15], [18], [20], [25]. We summarize important developments below. First, the use of more sophisticated non-Lambertian reflectance maps in the SFS problem has been studied by quite a few researcher. Ikeuchi [10] used a double-delta specular model to determine orientations of a specular surface with photometric stereo images generated by distributed light sources. Coleman and Jain [2] used four light source photometric stereo images to extract the shape of textured and specular surfaces. Healy and Binford [7] and Tsai and Shah [29] employed the Torrance-Sparraw model in their work to determine the shape of a specular surface with a single image. Recently, Tagare and deFigueiredo [25] presented and analyzed a class of *m-lobed* non-Lambertian reflectance maps and developed a photometric stereo SFS method to determine the local surface normal and the reflectance map parameters. Second, the nearby point light source for the SFS problem was examined by Kim and Burger [13]. They derived a reflectance map with a nearby point light source under the orthographic projection and Lambertian surface assumptions, and determined local positions and orientations with photometric stereo images. Finally, the perspective projection model has been applied to the SFS problem by Penna [20], [21] and the authors [17]. Penna presented a local SFS analysis of a single perspective image of a Lambertian polyhedron-shaped surface, and proposed an algorithm which recovers the local shape of the polyhedron by solving a nonlinear system of algebraic equations. The potential extension of his method to a non-Lambertian object was also mentioned. However, this algorithm is practically unreliable due to its sensitivity to noise and numerical finite precision. Lee and Kuo [17] developed a more robust SFS algorithm based on a triangular element surface model and a linear approximation of a Lambertian reflectance map. It recovers the shape of a Lambertian surface

2

directly with single or multiple photometric stereo images taken under perspective projection.

Despite the above efforts, there has been no reflectance map model developed which removes all three constraints simultaneously. In this research, we derive a general physics-based reflectance map model which includes diffuse and specular reflection effects, a nearby point light source and perspective projection, and then develop a new unified algorithm for recovering depth variables from shaded images with such a reflectance map. We employ the Torrance and Sparrow BRDF (bidirectional reflectance distribution function) to model diffuse and specular reflections of the reflectance map based on geometrical optics. Furthermore, we incorporate the nearby point light source and perspective projection in the model. The complete model is quite complicated where the brightness at a surface point in an image depends on many factors including the surface property parameters, the surface normal at that point, the light source direction, specular direction, the viewer direction, and the distance between the surface point and the light source. The SFS problem would be very difficult if we attempted to determine the surface orientation as well as the position of a surface point by solving the nonlinear image irradiance equation with this general reflectance map. However, the solution procedure can be greatly simplified by introducing a triangular element surface model for the discretization and parameterization of the image irradiance equation. Through such a procedure, we can express the resulting discrete nonlinear system of equations in terms of depth variables only, and recover the object shape by linearizing the equations and minimizing a quadratic cost functional. Since our method recovers depth variables directly, no integrability constraint is required.

The paper is organized as follows. In Section 2, we derive a general reflectance map model which takes the following factors into account: the specular and diffuse components of light reflection, a nearby point light source and perspective projection. We consider the discretization and parameterization of the nonlinear reflectance map based on a triangular element surface model in Section 3. We are able to simplify the discrete reflectance map for several special cases, and these simplifications are examined also in this section. The formulation and solution of the SFS problem is studied in Section 4. We perform numerical experiments with one or multiple photometric stereo images to demonstrate the performance of the derived physics-based reflectance map model and the proposed SFS algorithm in Section 5. Some concluding remarks are given in Section 6.

3

2 General Reflectance Map Model

We first review the BRDF consisting of both specular and diffuse reflections in Section 2.1. An expression for the incident irradiance due to a nearby point light source is derived, and the radiance of reflected light from a surface patch is expressed in terms of BRDF and the incident irradiance in Section 2.2. Imaging geometry with perspective projection is examined in Section 2.3. Then, by combining results in Sections 2.1-2.3, we obtain a general physics-based reflectance map model and the corresponding image irradiance equation in Section 2.4.

2.1 BRDF with Specular and Diffuse Components

We illustrate the reflection geometry used in this paper in Fig. 1, where r is the distance between a surface point P and a point light source S, n is the unit surface normal at P, i is the unit vector toward the light source, v is the unit vector toward the camera and h is the unit vector along the specular direction. By definition [26], the bisector of i and v specifies the specular direction so that we have

$$\mathbf{h} = \frac{\mathbf{i} + \mathbf{v}}{\|\mathbf{i} + \mathbf{v}\|}.$$

The ϑ_i, ϑ_v and α denote the angles between n and i, n and v, and n and h, respectively. The zenith and azimuth angles (θ, ϕ) with a proper subscript represent a unit vector in a given polar cordinate system. The irradiance L_i of a surface patch is defined as the incident flux density with unit $W \cdot m^{-2}$

$$L_i = \frac{d\Phi_i}{dA_s},$$

where $d\Phi_i$ denotes the incident flux (in terms of Watts or simply W) arriving at the surface patch of area dA_s from an infinitesimal solid angle $d\omega_i$ along the direction i. The radiance L_r is defined as the flux emitted per unit foreshortened area per unit solid angle with unit $W \cdot m^{-2} \cdot sr^{-1}$,

$$L_r = \frac{d^2\Phi_r}{dA_s \cos\vartheta_v \, d\omega_v},$$

where $d^2\Phi_r$ denotes the radiant flux emitted into an infinitesimal solid angle $d\omega_v$ (in terms of steradian or simply sr) along the direction v from the surface patch of area dA_s.

The bidirectional reflectance distribution function (BRDF) proposed by Nicodemous et al. [19] is a useful tool for characterizing light reflection from solid surfaces. It provides the information of the brightness of a surface patch with given viewing and illumination directions. By definition, it
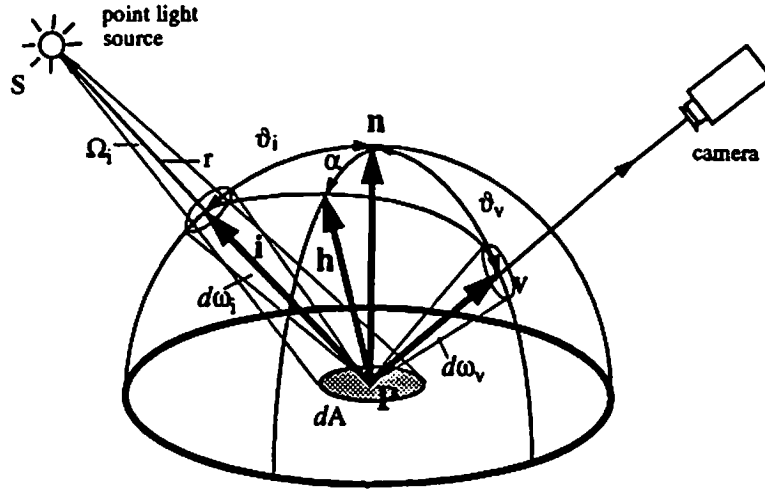
4

Figure 1:   The reflection geometry.

is written as

$$f_r = \frac{L_r}{L_i} \qquad (2.1)$$

where L_r and L_i denote the reflected radiance in the emitting direction and the irradiance in the direction of incident light, respectively. To model general light reflection from optically rough surfaces, the BRDF f_r consists of both the diffuse component f_d and the specular component f_s [18], [25], i.e.

$$f_r = \rho_d f_d + \rho_s f_s, \qquad (2.2)$$

where ρ_d and ρ_s are the weighting factors of diffuse and specular components.

Diffuse reflection is primarily due to internal scattering of the material, and obeys the Lambert's law in which the reflected radiance is proportional to the incident irradiance. The BRDF for Lambertian diffuse reflection is equal to a constant. That is,

$$f_d(\mathbf{i}, \mathbf{n}, \mathbf{v}) = \frac{1}{\pi}, \qquad (2.3)$$

A direct consequence of (2.3) is that the brightness L_r of a Lambertian surface is independent of the viewing direction $\mathbf{v}$. However, L_r does depend on $\mathbf{i}$ and $\mathbf{n}$ since L_i is a function of $\mathbf{i}$ and $\mathbf{n}$.

Specular reflection also contributes radiance reflected from the surface of an object. Two different methods have been proposed to model specular reflection, i.e. the physical optics and geometrical optics approaches. The physical optics approach [1] describes the interaction between incident light waves and the surface material with Maxwell's equations and the model is derived

5

by solving them with boundary conditions imposed with properties of the reflecting surface. Even though the model is accurate, it is very complicated. If the wavelength of incident light is much smaller than the dimension of surface irregularities [3], [23], [26], [27], it is more convenient to consider the geometrical optics approach. With this approach, a rough surface is modeled as a collection of planar facets which are inclined randomly about the mean surface. The surface facets are assumed to be isotropic and the distribution of facet orientations with respect to the mean surface normal can be described by a certain monotonically decreasing function such as the Phong [23], Torrance-Sparrow [26], and Trowbridge-Reitz [27] distribution functions. In this paper, we employ the Torrance-Sparrow distribution since it is mathematically simpler than that obtained by the physical optics approach and gives a better approximation than the Phong distribution. With the Torrance-Sparrow distribution, the BRDF of the specular components can be represented as

$$
\begin{aligned}
f_s(\mathbf{i}, \mathbf{n}, \mathbf{v}) &= \frac{1}{\cos\vartheta_i \cos\vartheta_v} \exp\{-k\alpha^2\} \\
&= \frac{1}{(\mathbf{i}^T\mathbf{n})(\mathbf{v}^T\mathbf{n})} \exp\{-k[\cos^{-1}(\mathbf{h}^T\mathbf{n})]^2\},
\end{aligned}
$$

where k is the surface roughness parameter.

2.2 Reflection Due to a Nearby Point Light Source

As indicated in (2.1), reflected radiance L_r depends on incident irradiance L_i as well as the BRDF f_r. Irradiance of a surface patch due to a nearby point light source will be examined in this section. Since the amount of light energy falling on a surface patch is proportional to the foreshortened area, the irradiance at that patch is proportional to a cosine function of the angle between the surface normal direction and the light source direction. Moreover, since the distance between the surface patch and the light source is finite, the irradiance is inversely proportional to square of the distance. Assume that the point light source has isotropic radiance I_0. Then, the corresponding solid angle Ω_i subtended by the surface patch dA_s viewed from the point light source is

$$
d\Omega_i = \frac{dA_s}{r^2} \max[0, \cos\vartheta_i],
$$

and the radiant flux intercepted by this solid angle is

$$
d\Phi_i = I_0 \, d\Omega_i = \frac{I_0}{r^2} dA_s \, \max[0, \cos\vartheta_i]. \tag{2.4}
$$

The averaged irradiance on the surface patch dA_s can be expressed as

$$
\frac{d\Phi_i}{dA_s} = \frac{I_0}{r^2} \max[0, \cos\vartheta_i] = \int_{-\pi}^{\pi} \int_0^{\pi/2} L_i(\theta_x, \phi_x) \sin\theta_x \, d\theta_x \, d\phi_x. \tag{2.5}
$$

6

Now, since the radiance of the point light source comes from only one direction i or (θ_i, ϕ_i), we can deduce from (2.5) that

$$L_i(\theta_x, \phi_x) = \frac{I_0}{r^2} \max[0, \cos \vartheta_i] \frac{\delta(\theta_x - \theta_i)\, \delta(\phi_x - \phi_i)}{\sin \theta_i}, \qquad (2.6)$$

where δ is the Dirac delta function. By defining a solid angle delta function [25]

$$\delta_\omega(\mathbf{x} - \mathbf{i}) = \delta_\omega(\theta_x - \theta_i, \phi_x - \phi_i) = \frac{\delta(\theta_x - \theta_i)\, \delta(\phi_x - \phi_i)}{\sin \theta_i},$$

we can write L_i in vector form as

$$L_i(\mathbf{x}, \mathbf{n}, r) = \frac{I_0}{r^2} \max[0, \mathbf{i}^T \mathbf{n}]\, \delta_\omega(\mathbf{x} - \mathbf{i}). \qquad (2.7)$$

Given a BRDF f_r of a surface and a point light source, the radiance of reflected light along the viewer direction v can be computed as

$$
\begin{aligned}
L_r(\mathbf{i}, \mathbf{n}, \mathbf{v}, r) &= \int_{\omega_x} f_r(\mathbf{x}, \mathbf{n}, \mathbf{v})\, L_i(\mathbf{x}, \mathbf{n}, r)\, d\omega_x \\
&= \int_{\omega_x} f_r(\mathbf{x}, \mathbf{n}, \mathbf{v}) \frac{I_0}{r^2} \max[0, \mathbf{i}^T \mathbf{n}]\, \delta_\omega(\mathbf{x} - \mathbf{i})\, d\omega_x \\
&= f_r(\mathbf{i}, \mathbf{n}, \mathbf{v}) \frac{I_0}{r^2} \max[0, \mathbf{i}^T \mathbf{n}].
\end{aligned}
\qquad (2.8)
$$

By substituting (2.2) into (2.8), we can represent the reflected hybrid radiance as

$$
\begin{aligned}
L_r(\mathbf{i}, \mathbf{n}, \mathbf{v}, r) &= [\rho_d f_d(\mathbf{i}, \mathbf{n}, \mathbf{v}) + \rho_s f_s(\mathbf{i}, \mathbf{n}, \mathbf{v})] \frac{I_0}{r^2} \max[0, \mathbf{i}^T \mathbf{n}] \\
&= \rho_d L_d(\mathbf{i}, \mathbf{n}, \mathbf{v}, r) + \rho_s L_s(\mathbf{i}, \mathbf{n}, \mathbf{v}, r),
\end{aligned}
\qquad (2.9)
$$

where

$$L_d = \frac{I_0}{r^2 \pi} \max[0, \mathbf{i}^T \mathbf{n}], \quad \text{and} \quad L_s = \frac{I_0}{r^2} \frac{\exp\{-k[\cos^{-1}(\mathbf{h}^T \mathbf{n})]^2\}}{(\mathbf{i}^T \mathbf{n})(\mathbf{v}^T \mathbf{n})} \max[0, \mathbf{i}^T \mathbf{n}]. \qquad (2.10)$$

are the diffuse and specular radiance components, respectively.

2.3 Imaging Geometry with Perspective Projection

Imaging geometry defines the mapping between a surface point and its corresponding projected point in the image plane. Besides, it relates image irradiance to scene radiance. The general perspective projection, which models the ideal pinhole camera, is employed in this work. As depicted in Fig. 2, we consider a camera-centered Cartesian coordinate system with the lens at the
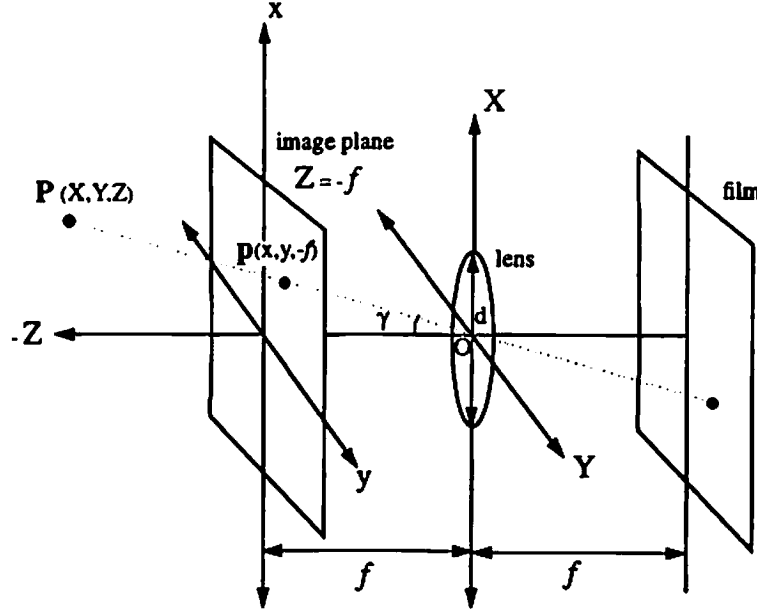
Figure 2:   The imaging geometry.

origin called the *center of projection* and the optical axis aligned with the $-Z$-axis. The actual film is located at $Z = f$ where f is the *focal length* behind the lens. However, to avoid the sign reversal of the coordinates, we assume without loss of generality that the image plane $x - y$ is located at $Z = -f$ in front of the lens. With this model, the mapping between a surface point $\mathbf{P} = (X, Y, Z)^T$ and the projected image point $\mathbf{p} = (x, y, -f)^T$ obeys the following relationship,

$$x = -f\frac{X}{Z}, \quad \text{and} \quad y = -f\frac{Y}{Z}. \tag{2.11}$$

The irradiance E at an image point of the film is obtained through the lens system via the radiance L_r of the corresponding surface point. It was shown in [9] that not all but only a portion of reflected light comes through the lens system which is known as the *lens collection* effect [6]. By assuming that the object distance is much larger than the focal length and the diameter of the lens and neglecting the transmission loss of the lens system, we can take the lens collection into account and have

$$E = \frac{\pi}{4}(\frac{d}{f})^2 \cos^4\gamma\, L_r, \tag{2.12}$$

where d is the diameter of the lens and γ is the angle between the ray from the object point to the center of projection and the optical axis.

8

2.4 Derived Reflectance Map Model and Image Irradiance Equation

As a direct consequence of (2.12), we can define the reflectance map function

$$R(\mathbf{i}, \mathbf{n}, \mathbf{v}, r) = \frac{\pi}{4} \left(\frac{d}{f}\right)^2 \cos^4\gamma \, L_r(\mathbf{i}, \mathbf{n}, \mathbf{v}, r), \qquad (2.13)$$

so that the image irradiance E at a point $\mathbf{p}$ in the image plane can be characterized by the image irradiance equation

$$E(\mathbf{p}) = R(\mathbf{i}(\mathbf{S}, \mathbf{P}), \mathbf{n}(\mathbf{P}), \mathbf{v}(\mathbf{P}), r(\mathbf{S}, \mathbf{P})), \qquad (2.14)$$

where the relatonship between the image point $\mathbf{p}$ and the corresponding surface point $\mathbf{P}$ is defined by the perspective law in (2.11). The cosine function of off-axis angle γ can be written as

$$\cos\gamma = -\mathbf{v}^T\mathbf{n}_z,$$

where $\mathbf{n}_z = (0, 0, 1)$ is the unit normal of X-Y plane. By substituting (2.9) and (2.10) into (2.13), the general reflectance map can be written as

$$
\begin{aligned}
R(\mathbf{i}, \mathbf{n}, \mathbf{v}, r) &= \frac{I_0}{r^2}(\mathbf{v}^T\mathbf{n}_z)^4 \frac{\pi}{4}\left(\frac{d}{f}\right)^2 \left(\frac{\rho_d}{\pi} + \rho_s\frac{\exp\{-k[\cos^{-1}(\mathbf{h}^T\mathbf{n})]^2\}}{(\mathbf{i}^T\mathbf{n})(\mathbf{v}^T\mathbf{n})}\right) \max[0, \mathbf{i}^T\mathbf{n}] \\
&= \begin{cases} \frac{I_0}{r^2}(\mathbf{v}^T\mathbf{n}_z)^4 \left(\beta_d\,\mathbf{i}^T\mathbf{n} + \beta_s\frac{\exp\{-k[\cos^{-1}(\mathbf{h}^T\mathbf{n})]^2\}}{\mathbf{v}^T\mathbf{n}}\right), & \mathbf{i}^T\mathbf{n} \geq 0, \\ 0, & \text{otherwise,} \end{cases}
\end{aligned}
$$

where β_d and β_s are constants of proper dimension that makes R a valid reflectance map. The values of β_d and β_s depend on the reflectivity of the object material, and can be estimated. We refer to [12] and [25] for more detailed discussion.

3 Discrete Reflectance Map Parameterized by Depth Variables

The SFS problem can be viewed as a problem of solving the image irradiance equation (2.14) with given (observed) image intensity at $\mathbf{p}$. The general reflectance map R in (2.13) is a function of the light source position $\mathbf{S}$, the position of a surface point $\mathbf{P}$ and the surface normal at that point which can be expressed as

$$\mathbf{n} = \frac{(-p, -q, 1)}{\sqrt{p^2 + q^2 + 1}}, \quad \text{where} \quad p = \frac{Z(X,Y)}{\partial X}, \quad q = \frac{Z(X,Y)}{\partial Y}.$$

Once the light source position and the projected point $\mathbf{p}$ in the image plane are specified, R reduces to a function of three variables, i.e. the depth Z and the gradients p and q, since the components

of **P** can be represented in terms of Z by the perspective law with known **p**. Thus, we are lead to a problem of solving three dependent variables Z, p and q characterizing the underlying surface with one given equation. To solve them uniquely, conventional photometric stereo methods use additional image irradiance equations due to other light sources as constraints [13], [25]. This approach has one difficulty, namely, since the variables Z, p and q are viewed as independent variables, the recovered depth variables and surface normals are often inconsistent. This is known as the integrability problem. Note also that the idea of using discrete approximations of p and q by a straightforward finite difference method, which has been applied to the orthographic SFS problem [14], [28], is no longer applicable in this context since the position components (X, Y) are in fact functions of the depth Z.

By introducing a triangular element surface model, we represent the surface normal as functions of the nodal depth. Consequently, the reflectance map R can be discretized and parameterized with only the nodal depth variables. Such a procedure greatly simplify the SFS problem formulation and its solution.

3.1 Discretization and Parameterization with Triangular Element Surface Model

Our basic idea of discretization and parameterization is to approximate a smooth object surface by the union of triangular surface patches called *triangular elements* such that the approximating surface can be written as a linear combination of a set of nodal basis functions of compact support. Let us triangulate a square image domain Ω by dividing it into a set of M_t nonoverlapping triangles T_i, $i = 1, \ldots, M_t$, with M_n nodal points p_i, $i = 1, \ldots, M_n$ so that the intensity within each triangle is almost homogeneous. Then, we approximate a smooth object surface by a piecewise linear surface consisting of triangular surface patches S_i with nodal points $\mathbf{P}_i$ in such a way that S_i and $\mathbf{P}_i$ are perspectively projected to T_i and p_i, respectively, in the image plane. The aproximating surface can be uniquely specified by $\mathbf{P}_i$, or equivalently the surface nodal depth variables Z_i associated with p_i, $i = i = 1, \ldots, M_n$.

Let us now focus on a triangular surface patch S_k and the corresponding projected triangle T_k on the image plane as shown in Fig. 3. We denote the nodal vectors (control points) of three vertices of S_k as

$$\mathbf{P}_i = (X_i, Y_i, Z_i), \quad \mathbf{P}_j = (X_j, Y_j, Z_j), \quad \mathbf{P}_l = (X_l, Y_l, Z_l),$$
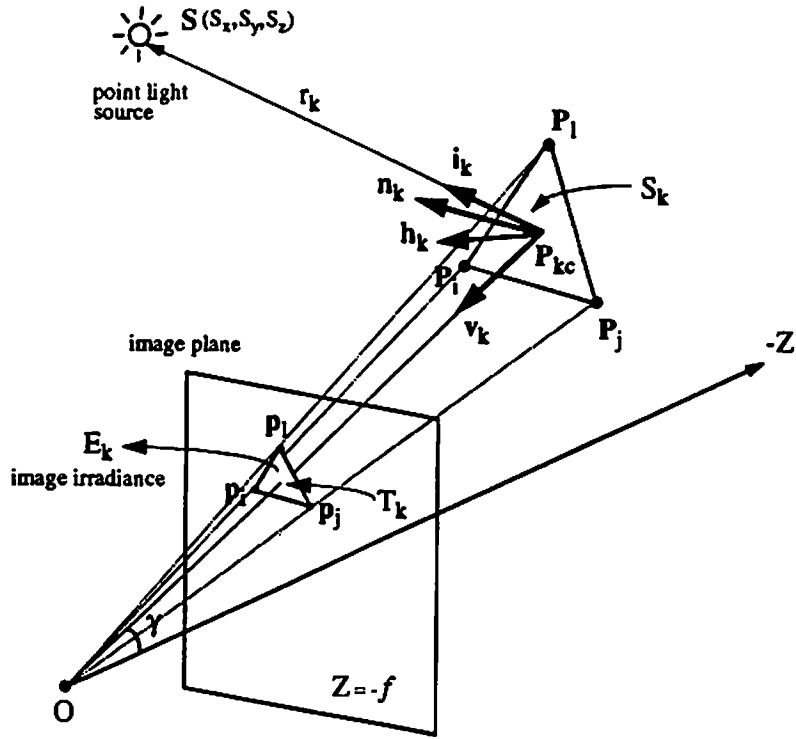
Figure 3: Projection of a triangular surface patch to the image plane.

and the corresponding projected nodal points in the image plane as

$$\mathbf{p}_i = (x_i, y_i, -f), \quad \mathbf{p}_j = (x_j, y_j, -f), \quad \mathbf{p}_l = (x_l, y_l, -f).$$

The center of S_k is

$$\mathbf{P}_{kc} = (X_{kc}, Y_{kc}, Z_{kc}) = (\frac{X_i + X_j + X_l}{3}, \frac{Y_i + Y_j + Y_l}{3}, \frac{Z_i + Z_j + Z_l}{3}).$$

By using the perspective relationship in (2.11), we can rewrite the components of $\mathbf{P}_{kc}$ in matrix form as

$$\begin{pmatrix} X_{kc} \\ Y_{kc} \\ Z_{kc} \end{pmatrix} = \frac{-1}{3f} \begin{pmatrix} x_i & x_j & x_l \\ y_i & y_j & y_l \\ -f & -f & -f \end{pmatrix} \begin{pmatrix} Z_i \\ Z_j \\ Z_l \end{pmatrix}.$$

We assume that f is known and the points (x_i, y_i), (x_j, y_j) and (x_l, y_l) are observed in the image plane. Then, $\mathbf{P}_{kc}$ depends only on the depth values of three nodal points Z_i, Z_j and Z_l. The unit vector $\mathbf{i}_k$ of the light source direction at the center of the surface patch S_k can be written as

$$\mathbf{i}_k = \frac{1}{r_k}(\mathbf{S} - \mathbf{P}_{kc}) = \frac{1}{r_k}(S_x - X_{kc}, S_y - Y_{kc}, S_z - Z_{kc}),$$

11

where

$$r_k = \|\mathbf{S} - \mathbf{P}_{kc}\| = [(S_x - X_{kc})^2 + (S_y - Y_{kc})^2 + (S_z - Z_{kc})^2]^{1/2} \qquad (3.1)$$

is the distance between the light source S and $\mathbf{P}_{kc}$. Similarly, the unit vector $\mathbf{v}_k$ along the viewing directon from the surface patch S_k can be represented by

$$\mathbf{v}_k = \frac{\mathbf{O} - \mathbf{P}_{kc}}{\|\mathbf{O} - \mathbf{P}_{kc}\|} = \frac{1}{(X_{kc}^2 + Y_{kc}^2 + Z_{kc}^2)^{1/2}}(-X_{kc}, -Y_{kc}, -Z_{kc}). \qquad (3.2)$$

The unit vector $\mathbf{h}_k$ along the specular direction on S_k can also be determined by

$$\mathbf{h}_k = \frac{\mathbf{i}_k + \mathbf{v}_k}{\|\mathbf{i}_k + \mathbf{v}_k\|}.$$

Besides, the surface normal $\mathbf{n}_k$ of the triangular surface patch S_k can be uniquely determined by its three nodal vectors $\mathbf{P}_i$, $\mathbf{P}_j$ and $\mathbf{P}_l$ via

$$
\begin{aligned}
\mathbf{n}_k &= \frac{(\mathbf{P}_j - \mathbf{P}_i) \times (\mathbf{P}_l - \mathbf{P}_i)}{|\,(\mathbf{P}_j - \mathbf{P}_i) \times (\mathbf{P}_l - \mathbf{P}_i)\,|} \\
&= \frac{(X_j - X_i, Y_j - Y_i, Z_j - Z_i) \times (X_l - X_i, Y_l - Y_i, Z_l - Z_i)}{|\,(X_j - X_i, Y_j - Y_i, Z_j - Z_i) \times (X_l - X_i, Y_l - Y_i, Z_l - Z_i)\,|}. \qquad (3.3)
\end{aligned}
$$

By using the perspective relationship in (2.11), we can rewrite $\mathbf{n}_k$ in terms of the location of the image points as

$$
\begin{aligned}
\mathbf{n}_k &= \frac{(\frac{1}{f}(x_iZ_i - x_jZ_j), \frac{1}{f}(y_iZ_i - y_jZ_j), Z_j - Z_i) \times (\frac{1}{f}(x_iZ_i - x_lZ_l), \frac{1}{f}(y_iZ_i - y_lZ_l), Z_l - Z_i)}{|\,(\frac{1}{f}(x_iZ_i - x_jZ_j), \frac{1}{f}(y_iZ_i - y_jZ_j), Z_j - Z_i) \times (\frac{1}{f}(x_iZ_i - x_lZ_l), \frac{1}{f}(y_iZ_i - y_lZ_l), Z_l - Z_i)\,|} \\
&= \frac{(-\varphi_k, -\nu_k, \mu_k)^T}{(\varphi_k^2 + \nu_k^2 + \mu_k^2)^{1/2}},
\end{aligned}
$$

where

$$
\begin{pmatrix} \varphi_k \\ \nu_k \\ \mu_k \end{pmatrix} = \begin{pmatrix} f(y_i - y_j) & f(y_l - y_i) & f(y_j - y_l) \\ f(x_j - x_i) & f(x_i - x_l) & f(x_l - x_j) \\ (x_iy_j - x_jy_i) & (x_ly_i - x_iy_l) & (x_jy_l - x_ly_j) \end{pmatrix} \begin{pmatrix} Z_iZ_l \\ Z_iZ_j \\ Z_lZ_j \end{pmatrix}.
$$

Note that since the vectors $\mathbf{i}_k$, $\mathbf{v}_k$, $\mathbf{n}_k$, $\mathbf{h}_k$ and r_k are all expressed in terms of Z_i, Z_j and Z_l in the above discussion, the reflectance map R_k is only a function of Z_i, Z_j and Z_l, i.e. the depth variables of three vertices of S_k.

Finally, by using the image irradiance equation, we can relate the image intensity E_k of a triangle T_k directly to the nodal depth values of the corresponding surface patch S_k:

$$
\begin{aligned}
E_k &= R_k(\mathbf{i}_k, \mathbf{n}_k, \mathbf{v}_k, r_k) \\
&= \begin{cases} \frac{I_0}{r_k^2}(\mathbf{v}_k^T\mathbf{n}_x)^4\,(\beta_d\,\mathbf{i}_k^T\mathbf{n}_k + \beta_s\frac{\exp\{-k[\cos^{-1}(\mathbf{h}_k^T\mathbf{n}_k)]^2\}}{\mathbf{v}_k^T\mathbf{n}_k}), & \mathbf{i}_k^T\mathbf{n}_k \geq 0, \\ 0, & \text{otherwise,} \end{cases} \qquad (3.4) \\
&= R_k(Z_i, Z_j, Z_l)
\end{aligned}
$$

3.2 Special Cases

We discuss several simplified reflectance map models for some special cases below.

3.2.1 Distant Light Source

If the light source is located far away from the object and the camera, the relative depth difference between surface points is negligible compared to the average distance from the object to the light source. For this case, the radiant flux in (2.4) arriving at a surface patch can be approximated as

$$d\Phi_i = \frac{I_0}{r^2} dA_s \, \max[0, \cos\vartheta_i] \approx I_l \, dA_s \, \max[0, \cos\vartheta_i], \tag{3.5}$$

where

$$\frac{I_0}{r^2} \approx I_l \equiv I_0/\bar{r}^2,$$

and where $\bar{r}$ is the average distance between the object surface and the light source. Besides, since the light source is far away, we can assume that incident rays from the light source are in parallel with each other. Then, the unit vector $\mathbf{i}_k$ of the light source direction in (3.1) is independent of the position of the surface patch so that we can drop the subscription and approximate it as

$$\mathbf{i} \approx \frac{\mathbf{S} - \mathbf{O}}{\|\mathbf{S} - \mathbf{O}\|} = \frac{(S_x, S_y, S_z)}{(S_x^2 + S_y^2 + S_z^2)^{1/2}}. \tag{3.6}$$

3.2.2 Distant Object

When an object is far away from the camera while the light source is near the object, the perspective projection model can be approximated by the simpler orthographic projection model. With orthogonal projection, we have the following relationship,

$$x = X, \quad y = Y. \tag{3.7}$$

For this case, since all rays from the surface points are in parallel with each other and orthogonal to the image plane, the unit vector $\mathbf{v}_k$ along the viewer direction from the surface patch S_k in (3.2) becomes independent on the position of the patch, i.e.

$$\mathbf{v}_k = \mathbf{v} = \mathbf{n}_z = (0, 0, 1)^T. \tag{3.8}$$

Moreover, since

$$\cos\gamma = -\mathbf{n}_z^T \mathbf{n}_z = -1, \tag{3.9}$$

13

the lens collection is independent on the surface position and (2.12) reduces to

$$E = CL_r,$$

where C is the constant collection factor $\pi d^2/(4f^2)$. Besides, by using the orthographic projection relationship in (3.7), the surface normal in (3.3) can be approximated by

$$
\begin{aligned}
\hat{\mathbf{n}}_k &= \frac{(x_j - x_i, y_j - y_i, Z_j - Z_i) \times (x_l - x_i, y_l - y_i, Z_l - Z_i)}{|(x_j - x_i, y_j - y_i, Z_j - Z_i) \times (x_l - x_i, y_l - y_i, Z_l - Z_i)|}, \\
&= \frac{(-\hat{\varphi}_k, -\hat{\nu}_k, \hat{\mu}_k)^T}{(\hat{\varphi}_k^2 + \hat{\nu}_k^2 + \hat{\mu}_k^2)^{1/2}},
\end{aligned}
\tag{3.10}
$$

where

$$
\begin{aligned}
\hat{\varphi}_k &= (y_j - y_l)Z_i + (y_i - y_j)Z_l + (y_l - y_i)Z_j, \\
\hat{\nu}_k &= (x_l - x_j)Z_i + (x_j - x_i)Z_l + (x_i - x_l)Z_j, \\
\hat{\mu}_k &= (x_j y_l - x_l y_j) + (x_i y_j - x_j y_i) + (x_l y_i - x_i y_l).
\end{aligned}
$$

3.2.3 Distant Light Source and Object

If the light source, the object and the camera are far away from one another, both the distant light point source and orthographic projection assumptions hold. For this case, the vectors $\mathbf{i}_k, \mathbf{v}_k$ and $\mathbf{h}_k$ are no longer dependent on the surface position. Once the light source direction is specified, the brightness of a pixel in an image plan is determined only by the surface normal $\mathbf{n}_k$. By using (3.5), (3.6), (3.8), (3.9), (3.10) and dropping off the unnecessary subscripts, we obtain the simplified reflectance map

$$
R_k(\mathbf{i}, \hat{\mathbf{n}}_k, \mathbf{v}) = \begin{cases} I_l \left(\beta_d \, \mathbf{i}^T \hat{\mathbf{n}}_k + \beta_s \dfrac{\exp\{-k[\cos^{-1}(\mathbf{h}^T \hat{\mathbf{n}}_k)]^2\}}{\mathbf{v}^T \hat{\mathbf{n}}_k} \right), & \mathbf{i}^T \hat{\mathbf{n}}_k \geq 0, \\ 0, & \text{otherwise}, \end{cases}
$$

and where V_k denotes the index set of vertices of T_k.

4 Formulation of the SFS Problem

The shape of an object, which is approximated with a union of linear triangular surface patches, can be characterized by the coordinates of the nodal points $\mathbf{P}_m = (X_m, Y_m, Z_m)$, $m = 1, \ldots, M_n$. Since the positions of the points $\mathbf{p}_m = (x_m, y_m, -f)$, $m = 1, \ldots, M_n$ in the image plane are given, one can determine the positions of $\mathbf{P}_m$ by calculating the nodal depths Z_m, $m = 1, \ldots, M_n$ and applying the perspective law (2.11) to find out the corresponding X_m and Y_m. The reflectance map R_k given by (3.4) is a nonlinear function of depth variables Z_i, Z_j and Z_l which makes the

14

SFS problem difficult to solve. However, we can simplify the solution process by linearizing the reflectance map, solving the linearized problem, and then applying a successive linearization scheme to improve the accuracy of the computed solution.

By successive linearization, we mean that the nodal values obtained from the previous iteration are used as the reference points for linearization for the current iteration. In terms of mathematics, we can derive a linear approximation of R_k at the nth iteration by taking the Taylor series expansion about the reference depth values obtained at the $(n-1)$th iteration as

$$
\begin{aligned}
R_k(Z_i&, Z_j, Z_l) \\
&\approx R_k(Z_i^{n-1}, Z_j^{n-1}, Z_l^{n-1}) + \sum_{m=i,j,l} (Z_m - Z_m^{n-1}) \frac{\partial R_k(Z_i, Z_j, Z_l)}{\partial Z_m} \bigg|_{(Z_i^{n-1}, Z_j^{n-1}, Z_l^{n-1})} \\
&= \sum_{m=i,j,l} \frac{\partial R_k(Z_i, Z_j, Z_l)}{\partial Z_m} \bigg|_{(Z_i^{n-1}, Z_j^{n-1}, Z_l^{n-1})} Z_m \\
&\quad + \left\{ R_k(Z_i^{n-1}, Z_j^{n-1}, Z_l^{n-1}) - \sum_{m=i,j,l} \frac{\partial R_k(Z_i, Z_j, Z_l)}{\partial Z_m} \bigg|_{(Z_i^{n-1}, Z_j^{n-1}, Z_l^{n-1})} Z_m^{n-1} \right\}.
\end{aligned}
$$

Since the second term of the above equation is equal to a constant, the reflectance map R_k over S_k is a linear function of depth values Z_i, Z_j and Z_l of the three vertices of S_k. We may rewrite R_k in terms of all nodal depth variables Z_m, $m = 1, \ldots, M_n$. That is,

$$
R_k \approx \sum_{m=1}^{M_n} \omega_{km} Z_m + \xi_k, \tag{4.1}
$$

where

$$
\omega_{km} = \begin{cases} \dfrac{\partial R_k(Z_i, Z_j, Z_l)}{\partial Z_m} \bigg|_{(Z_i^{n-1}, Z_j^{n-1}, Z_l^{n-1})}, & \text{if } m \in V_k = \{i, j, l\} \text{ of } T_k, \\ 0, & \text{otherwise,} \end{cases} \tag{4.2}
$$

and

$$
\xi_k = R_k(Z_i^{n-1}, Z_j^{n-1}, Z_l^{n-1}) - \sum_{m=1}^{M_n} \omega_{km} Z_m^{n-1}. \tag{4.3}
$$

Our objective is to determine the nodal depth Z_m with one or multiple images. To achieve this goal, we employ a cost functional minimization approach with J different photometric stereo images taken by various illumination directions while keeping the camera position fixed. The scheme reduces to the single image SFS algorithm for $J = 1$. The cost functional is chosen to be

$$
\mathcal{E} = \sum_{k=1}^{M_t} \sum_{j=1}^{J} \mathcal{E}_k^j = \sum_{k=1}^{M_t} \sum_{j=1}^{J} (E_k^j - R_k^j)^2, \tag{4.4}
$$

15

where $\mathcal{E}_k^j$ denotes the cost term corresponding to the kth triangular domain of the jth image, and E_k^j and R_k^j are the observed image irradiance and the reflectance map over the kth triangular domain of the jth image, respectively. It is worthwhile to emphasize that no regularization term is used in (4.4).

By substituting (4.1) into (4.4) and simplifying the expression, we obtain

$$
\begin{aligned}
\mathcal{E} &= \sum_{k=1}^{M_t} \sum_{j=1}^{J} [E_k^j - (\sum_{m=1}^{M_n} \omega_{km}^j Z_m + \xi_k^j)]^2 \\
&= \frac{1}{2} \mathbf{z}^T \mathbf{A} \mathbf{z} - \mathbf{b}^T \mathbf{z} + c, \quad \mathbf{z} = [Z_1, Z_2, \dots, Z_{M_n}]^T,
\end{aligned} \tag{4.5}
$$

where the stiffness matrix $\mathbf{A}$ and the load vector $\mathbf{b}$ are the sum of each individual stiffness matrix $\mathbf{A}_j$ and the load vector $\mathbf{b}_j$ of jth image, respectively. In terms of mathematics, we have

$$
\mathbf{A} = \sum_{j=1}^{J} \mathbf{A}_j, \quad \text{and} \quad \mathbf{b} = \sum_{j=1}^{J} \mathbf{b}_j,
$$

where the individual stiffness matrix $\mathbf{A}_j$ and the load vector $\mathbf{b}_j$ can be determined by

$$
[\mathbf{A}_j]_{m,n} = 2 \sum_{k=1}^{M_t} \omega_{km}^j \omega_{kn}^j, \quad \text{and} \quad [\mathbf{b}_j]_m = 2 \sum_{k=1}^{M_t} (E_k^j - \xi_k^j) \omega_{km}^j, \quad 1 \le m, n \le M_n,
$$

and where ω^j and ξ^j are the coefficients in (4.2) and (4.3) for the jth image. The minimization of the quadratic functional in (4.5) with respect to the nodal variables $\mathbf{z}$ is equivalent to the solution of a linear system of equations

$$
\mathbf{A}\mathbf{z} = \mathbf{b}.
$$

Since the stiffness matrix $\mathbf{A}$ is sparse and symmetric, the system can be efficiently solved by iterative methods such as the multigrid method and the preconditioned conjugate gradient method [5], [24].

5 Experimental Results

We present some experimental results to demonstrate the performance of the proposed SFS algorithm in this section. In the experiment, we put light sources on the $Z = 0$ plane centered around the origin. When two light sources are used, they are chosen to be orthogonal to each other in the azimuth angle, and when three are used, they are placed to be 120° apart in the azimuth angle. Unless specified otherwise, the initial depth estimates Z_i^0, $i = 1, \dots M_n$ are set to be an arbitrary constant and no a priori knowledge about the true depth is assumed. Since the nodal points whose

16

depth values can be determined by the SFS algorithm are irregular and sparse on the object domain, we perform interpolation to increase the resolution and visibility of the reconstructed surface.

Test Problem 1: Spherical polyhedron

We examine the performance of the proposed algorithm applied to a spherical polyhedron whose surface is composed of piecewise triangular patches so that it fits the model described in Section 3.1. The 17×17 surface depth values associated with image nodal points are shown in Fig. 4(a). The ideal image intensity E_k of each triangle T_k with respect to each triangular surface patch S_k can be exactly determined by (3.8) so that E_k contains no noise except quantization error. We set the focal length $f = 30$, the source radiance $I_0 = 1.5 \times 10^6$, the diffuse and specular weighting factors $\beta_d = 0.6$, $\beta_s = 0.4$ and the surface roughness parameter $k = 10$, respectively.

The recovered surface depth values with a single image generated by a light source located at $(S_x, S_y, S_z) = (52, 30, 0)$ is shown in Fig. 4(b). The result with two photometric stereo images generated by two light sources $(S_x, S_y, S_z) = (52, 30, 0)$ and $(-30, 52, 0)$ is shown in Fig. 4(c). We also show in Fig. 4(d) the reconstructed surface with three photometric stereo images with light sources at $(S_x, S_y, S_z) = (60, 0, 0)$, $(-30, 52, 0)$ and $(-30, -52, 0)$. To see the accuracy of the recovery results more clearly, we present the 1-D sliced view of three reconstructed surfaces along with the original one in Fig. 4(e), where the solid, dotted, dashdot, and '+' marked lines are used to represent the ground truth and the results depicted in Figs. 4 (b), (c) and (d), respectively. In this experiment, we set the initial surface to be the plane $Z = -100$. Our algorithm is in fact very robust and not sensitive to the initial condition and it converges to a unique solution. We observe from the results in Fig. 4 that a single image does not provide accurate depth information. Moreover it is interesting to see that unlike the Lambertian case where two images are sufficient to recover accurate results [15], [17], non-Lambertian surface can hardly be recovered correctly with two photometric stereo images. The result in Fig. 4 shows that with three photometric stereo images, we can obtain quite robust and accurate reconstructions of the non-Lambertian test surface. However, we observe that when the specular factor β_s or the surface roughness k becomes very large, the accuracy of the reconstructed depth even with three images becomes degraded.

Test Problem 2: Sphere

We synthesize test images by illuminating a 129×129 spherical surface as shown in Fig. 5(a) via a pointwise mapping of (2.14) with the surface normal approximated by

$$\mathbf{n} = \frac{(-p, -q, 1)^T}{\sqrt{p^2 + q^2 + 1}}, \quad \text{where} \quad p = Z(X + 1, Y) - Z(X, Y), \quad q = Z(X, Y + 1) - Z(X, Y),$$

17

and estimate the average intensity E_k of each image triangle T_k on the tessellated image domain as discussed in [17]. By setting $f = 200$ and $I_0 = 5.6 \times 10^7$, we obtain a set of test images of size 64×64 by varying both surface reflection parameters and the source position as shown in Figs. 5(b)-(g). Figs. 5(b) and (c) are two photometric stereo images of a Lambertian surface ($\beta_d = 1, \beta_s = 0$) with light sources at $(S_x, S_y, S_z) = (-150, 260, 0)$ and $(260, 150, 0)$, while Figs. 5(d)-(g) are those of a hybrid surface with $(\beta_d, \beta_s, k) = (0.5, 0.5, 7)$ and light sources at $(S_x, S_y, S_z) = (-150, 260, 0)$, $(-260, 150, 0)$, $(260, 150, 0)$ and $(0, -300, 0)$, respectively.

Figs. 6(a) and (b) show the reconstructed Lambertian and non-Lambertian surfaces by using a Lambertian reflectance map model with two sets of photometric stereo images in Figs. 5(b) and (c) and Figs. 5(d) and (f), respectively. The results of applying the Lambertian reflectance map and the general reflectance map to three photometric images of the hybrid surface in Figs. 5(e), (f) and (g) are shown in Figs. 6(c) and (d), respectively. By comparing the results in Figs. 6(b), (c) an (d), we see clearly that applying the Lambertian model to a non-Lambertian hybrid surface produces a substantial amount of reconstruction error, and is thus not appropriate in practice.

In Figs. 6(e) and (f), we show the 1-D sliced view of reconstructed surfaces, where the solid lines denote the ground truth while the dotted lines represent results by using correct reflectance maps (i.e. results in Figs. 6(a) and (d)). Compared to the absolute depth of the ground truth, the reconstructed surfaces are shifted globally by a certain amount. By referring the results of the ideal case in Fig. 4(c), this discrepancy is primarily due to the noise caused by estimating the image intensity E_k via a averaging process. However, this depth discrepancy can be reduced by incorporating the depth information of a single surface point. We used $Z(0,0) = -380$, the depth of the center point, as a hard constraint. We show the results in Figs. 6(e) and (f) with dashed lines. It is clear from these figures that almost exact depth is reconstructed by using three photometric stereo images with a depth constraint.

Test Problem 3: Cylinder

The test object is a cylindrical surface as shown in Fig. 7(a). Figs. 7(b)-(d) are the test images synthesized with parameters $f = 200$, $I_0 = 5.6 \times 10^7$, $\beta_d = 0.5$, $\beta_s = 0.5$, $k = 10$ and light sources at $(S_x, S_y, S_z) = (260, 150, 0)$, $(-260, 150, 0)$ and $(0, -300, 0)$, respectively. The recovered depth by applying the Lambertian reflectance map to this hybrid surface with the three test images are shown in Fig. 8(a) while Figs. 8(b) and (c) show the recovered depth of using the general reflectance map without and with a depth constraint $Z(0,0) = -380$, respectively. We also show the 1-D slice plot in Fig. 8(d) to illustrate the accuracy of reconstructed surfaces, where the solid, dashdot, dotted

and dashed lines are used to represent the ground truth and the results depicted in Figs. 8 (a), (b) and (c), respectively. We see that the error of applying the Lambertian model to a hybrid surface is obvious and the general reflectance map model with a depth constraint gives the almost exact reconstruction.

Test Problem 4: Penny

The Penny surface is shown in Fig. 9 (a), and test images synthesized with parameters $f = 250$, $I_0 = 9.0 \times 10^7$, $\beta_d = 0.4$, $\beta_s = 0.6$, $k = 10$ and light sources at $(S_x, S_y, S_z) = (285, 285, 0)$, $(-386, 104, 0)$ and $(104, -386, 0)$, are given in Figs. 9(b)-(d), respectively. Fig. 10(a) is the reconstructed depth by applying the general reflectance map with a depth constraint $Z(0, 0) = -491$. In this case, the reconstruction error at the depth discontinuities is quite visible. For comparison, we show in Fig. 10(b) the 1-D slice plot of several reconstructed surfaces, where the solid, dashdot, dotted and dashed lines denote the ground truth and the results obtained by applying a Lambertian model, a general reflectance model without and with a depth constraint, respectively. Since the test surface is more complicate than the spherical and cylindrical surfaces with considerable local depth variation, the averaging effect in estimating E_k is more serious. This explains why the reconstructed surface with the general reflectance model but without using the depth constraint becomes worse for this problem than that of Test Problem 3.

6 Conclusion

A new general physics-based reflectance map model which includes diffuse and specular reflection effects, a nearby point light source and perspective projection was derived in this research. We discussed the discretization and parameterization of the derived reflectance map in terms of nodal depth variables by using a triangular element surface representation, and proposed a direct shape recovery algorithm from shaded images by successively linearizing the reflectance map and minimizing a quadratic cost functional. The proposed method is practically attractive, since it recovers a broad range of object surfaces with different reflective properties and under various geometric and lighting environments. We have used some experiments to demonstrate the excellent performance of the new method.

References

[1] P. Beckmann and A. Spizzichino, *The Scattering of Electromagnetic Waves from Rough Surfaces*, New York: Pergamon, 1963.

[2] E. N. Coleman Jr. and R. C. Jain, "Obtaining 3-dimensional shape of textured and specular surface using four-source photometry," *Computer Graphics and Image Processing*, Vol. 18, pp. 309–328, 1982.

[3] R. L. Cook and K. E. Torrance, "A reflectance model for computer graphics," *ACM computer Graphics*, Vol. 15, No. 3, pp. 307–316, 1981.

[4] P. Dupuis and J. Oliensis, "Direct method for reconstructing shape from shading," in *IEEE Conference on Computer Vision and Pattern Recognition*, (Champaign, Illinois), pp. 453–458, June 1992.

[5] W. Hackbusch, *Multi-Grid Methods and Applications*, Berlin: Springer-Verlag, 1985.

[6] R. M. Haralick and L. G. Shapiro, *Computer and robot vision*, Addison Wesley, 1992.

[7] G. Healey and T. O. Binford, "Local shape from specularity," *Computer Vision, Graphics, and Image Processing*, Vol. 42, pp. 62–86, 1988.

[8] B. K. P. Horn, "Height and gradient from shading," *International Journal of Computer Vision*, Vol. 5, pp. 584–595, 1990.

[9] B. K. P. Horn and R. W. Sjoberg, "Calculating the reflectance map," *Applied Optics*, Vol. 18, pp. 1770–1779, 1979. Also in *Shape from Shading*, B. K. P. Horn and M. J. Brooks (eds.) 1989, MIT Press, Cambridge, MA.

[10] K. Ikeuchi, "Determining surface orientations of specular surfaces by using the photometric stereo method," *IEEE Trans. Pattern Analysis and Machine Intelligence*, Vol. PAMI-3, No. 6, pp. 661–669, 1981.

[11] K. Ikeuchi and B. K. P. Horn, "Numerical shape from shading and occluding boundaries," *Artificial Intelligence*, Vol. 17, pp. 141–184, 1981. Also in *Shape from Shading*, B.K. P. Horn and M. J. Brooks (eds.) 1989, MIT Press, Cambridge, MA.

[12] K. Ikeuchi and K. Sato, "Determining reflectance properties of an object using range and brightness images," *IEEE Trans. Pattern Analysis and Machine Intelligence*, Vol. 13, No. 11, pp. 1139–1153, 1991.

[13] B. Kim and P. Burger, "Depth and shape from shading using the photometric stereo method," *Computer Vision, Graphics, and Image Processing: Image Understanding*, Vol. 54, No. 3, pp. 416–427, 1991.

[14] Y. G. Leclerc and A. F. Bobick, "The direct computation of height from shading," in *IEEE Conference on Computer Vision and Pattern Recognition*, (Hawaii), pp. 552–558, May 1991.

[15] K. M. Lee and C.-C. J. Kuo, "Shape from shading with perspective projection," Tech. Rep. 216, USC, Signal and Image Processing Institute, 1992. submitted for possible publication.

[16] K. M. Lee and C.-C. J. Kuo, "Shape from shading with a linear triangular element surface model," *IEEE Trans. Pattern Analysis and Machine Intelligence*, Vol. PAMI-15, July 1993.

[17] K. M. Lee and C.-C. J. Kuo, "Surface reconstruction from photometric stereo images," *Journal of Optical Society of America: A*, Vol. 10, No. 5, pp. 855–868, 1993.

[18] S. K. Nayar, K. Ikeuchi, and T. Kanade, "Surface reflection: physical and geometrical perspectives," *IEEE Trans. Pattern Analysis and Machine Intelligence*, Vol. 13, pp. 611–634, July 1991.

[19] F. E. Nicodemus, J. C. Richmond, J. J. Hsia, and I. W. Ginsberg, *Geometrical Considerations and Nomenclature for Reflectance*, Boulder CO: National Bureau of Standards, 1977.

[20] M. A. Penna, "Local and semi-local shape from shading for a single perspective image of a smooth object," *Computer Vision, Graphics, and Image Processing*, Vol. 46, pp. 346–366, 1989.

[21] M. A. Penna, "A shape from shading analysis for a single perspective image of a polyhedron," *IEEE Trans. Pattern Analysis and Machine Intelligence*, Vol. PAMI-11, pp. 545–554, June 1989.

[22] A. P. Pentland, "Shape information from shading: a theory about human perception," in *Proc. of International Cof. on Computer Vision*, pp. 404–413, 1988.

[23] B. T. Phong, "Illumination for computer generated pictures," *Communications of the ACM*, Vol. 18, pp. 311–317, June 1975.

[24] R. Szeliski, "Fast surface interpolation using hierarchical basis functions," *IEEE Trans. Pattern Analysis and Machine Intelligence*, Vol. 12, No. 6, pp. 513–528, 1990.

[25] H. D. Tagare and R. J. P. DeFigueiredo, "A theory of photometric stereo for a class of diffuse non-lambertian surface," *IEEE Trans. Pattern Analysis and Machine Intelligence*, Vol. 13, No. 2, pp. 133–152, 1991.

[26] K. E. Torrance and E. M. Sparrow, "Theory for off-specular reflection from roughened surfaces," *Journal of Optical Society of America*, Vol. 57, No. 9, pp. 1105–1114, 1967.

[27] T. S. Trowbridge and K. P. Reitz, "Average irregularity representation of a roughened surface for ray reflection," *Journal of Optical Society of America*, Vol. 65, pp. 531–536, 1975.

[28] P. S. Tsai and M. Shah, "A fast linear shape from shading," in *IEEE Conference on Computer Vision and Pattern Recognition*, (Champaign, Illinois), pp. 734–736, June 1992.

[29] P. S. Tsai and M. Shah, "A simple shape from shading algorithm," Tech. Rep. CS-TR-92-24, CS Dept, Univ. of Central Florida, 1992.

[30] R. J. Woodham, "Analyzing images of curved surfaces," *Artificial Intelligence*, Vol. 17, No. 1-3, pp. 117–140, 1981.
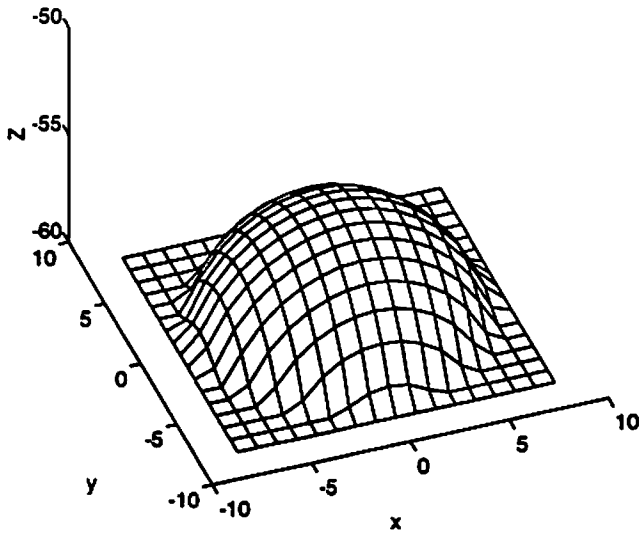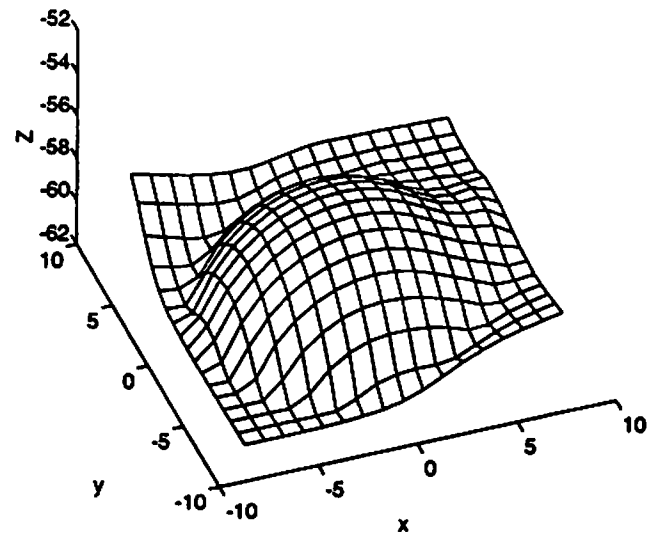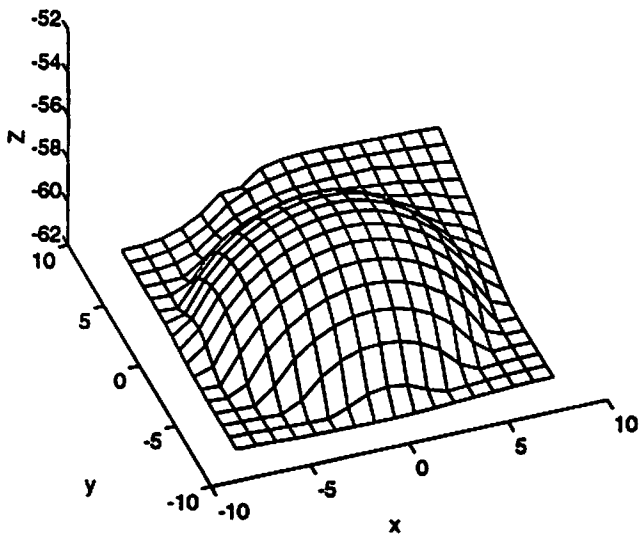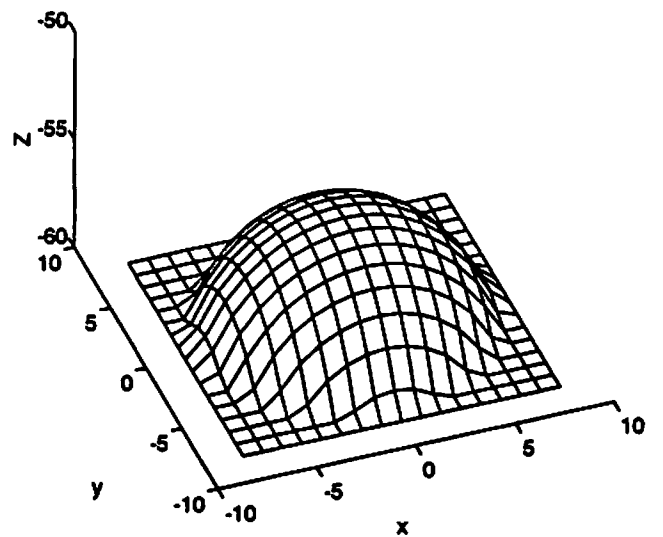
Figure 4: Test Problem 1: (a) ground truth, and reconstructed results with (b) a single image, (c) two photometric stereo images and (d) three photometric stereo images.

22
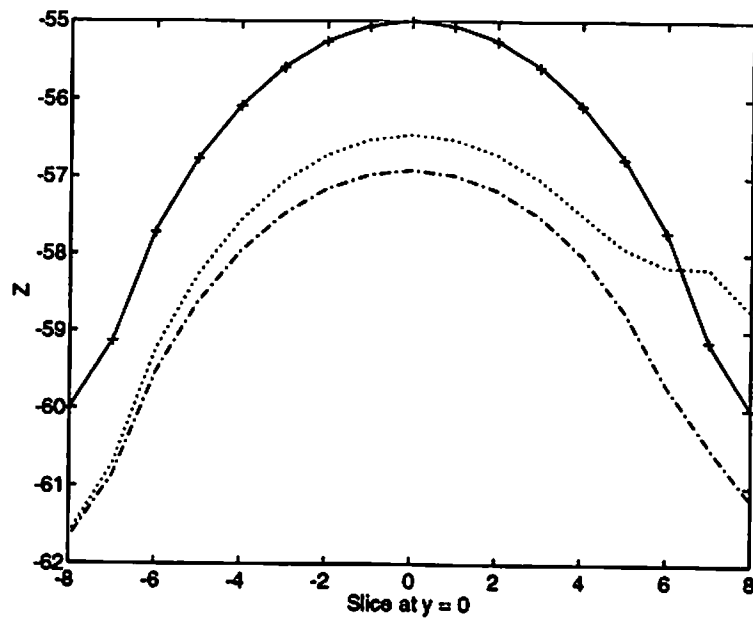
(d)

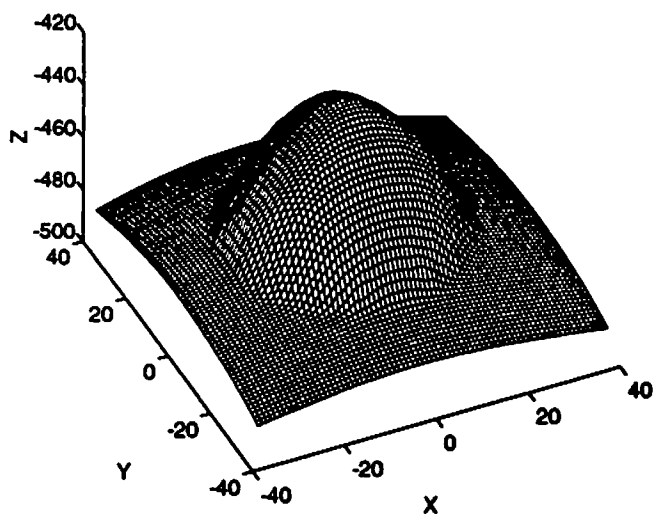Figure 4:   (Cont.) (e) the 1-D sliced plot of several reconstructed results.

23
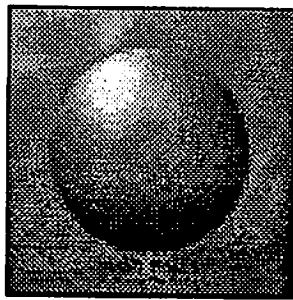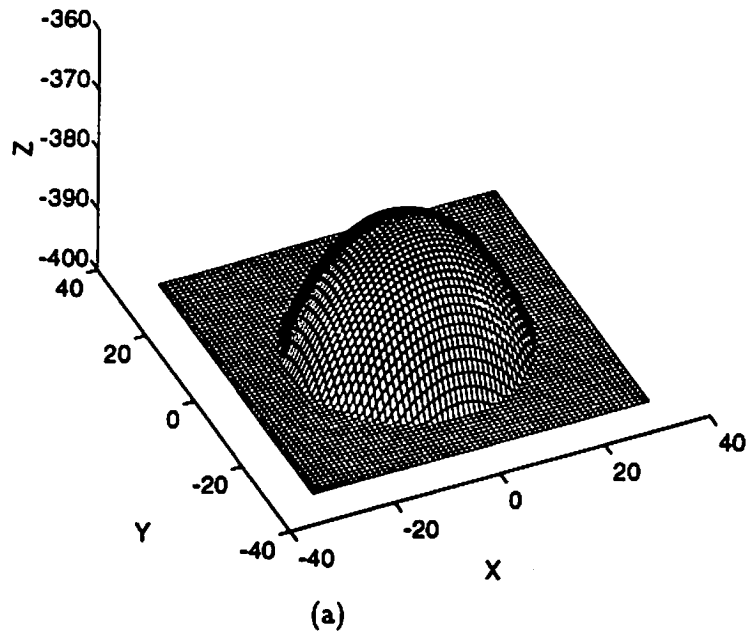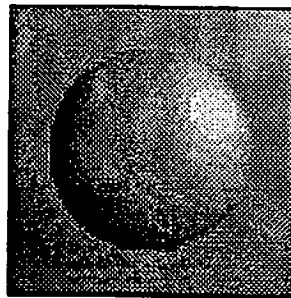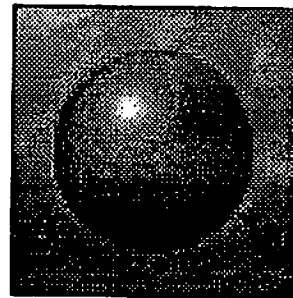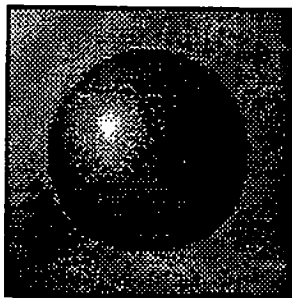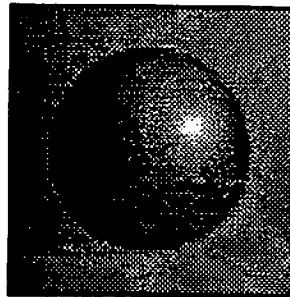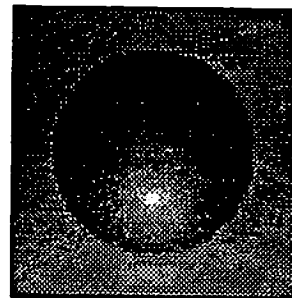
Figure 5: Test Problem 2: (a) ground truth of a spherical surface; (b) - (c) photometric stereo images of a Lambertian surface; (d) - (g) photometric stereo images of a hybrid surface.
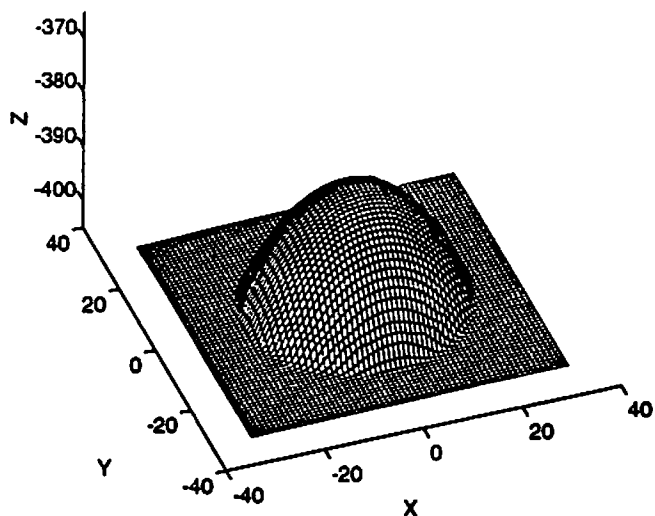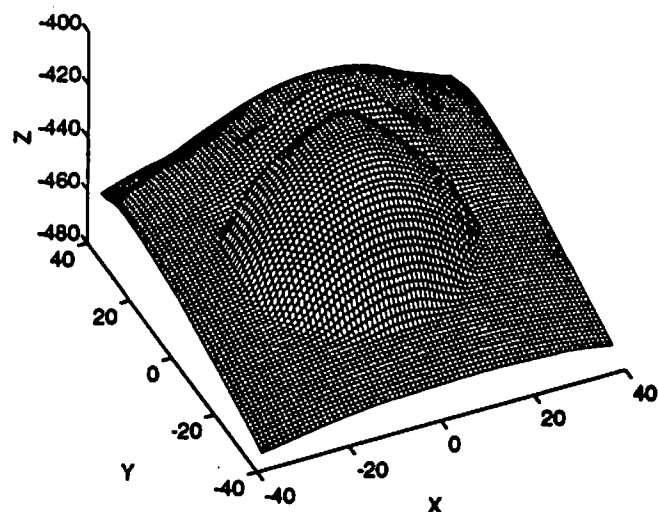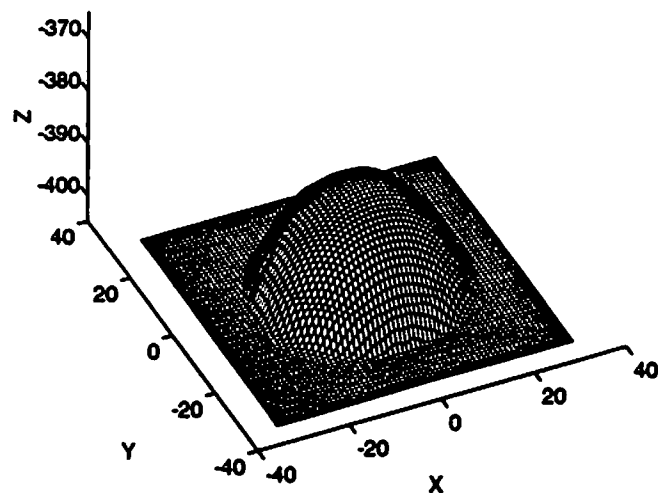
Figure 6: Reconstruction results of the spherical surface test problem: (a) applying the Lambertian model to two photometric stereo images of a Lambertian surface; (b) applying the Lambertian model to two photometric stereo images of a hybrid surface; (c) applying the Lambertian model to three photometric stereo images of a hybrid surface; (d) applying the general reflectance model to three photometric stereo images of a hybrid surface;

25
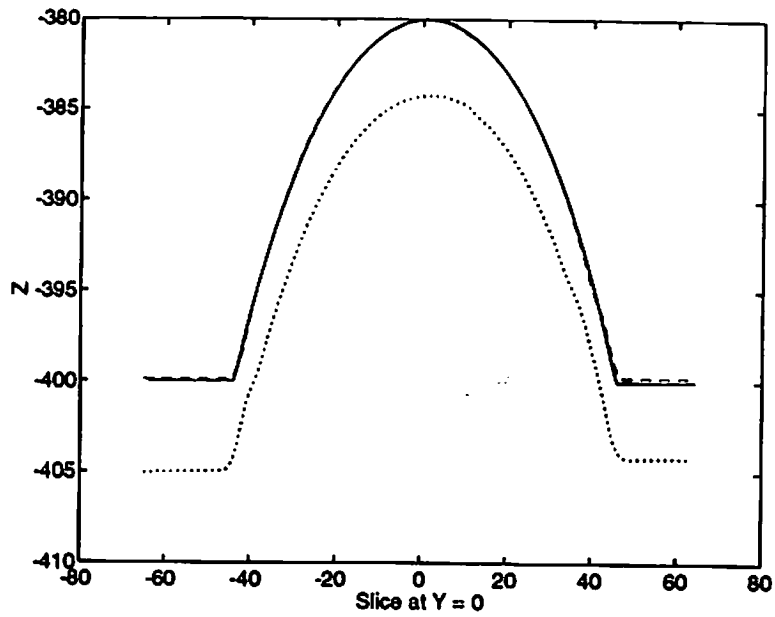
(e)
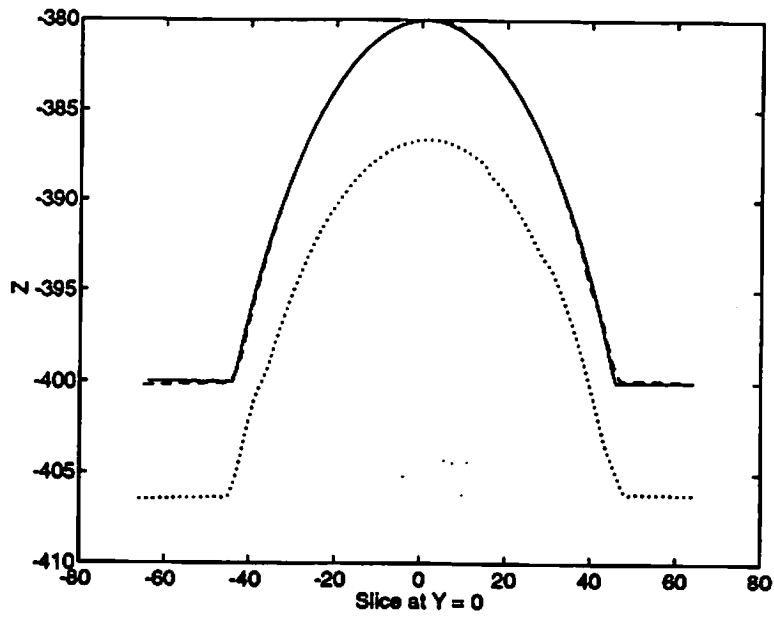
(f)

Figure 6: (Cont.): (e) 1-D sliced plot of reconstructed Lambertian surfaces, and (f) 1-D sliced plot of reconstructed hybrid surfaces.
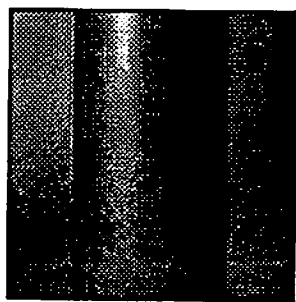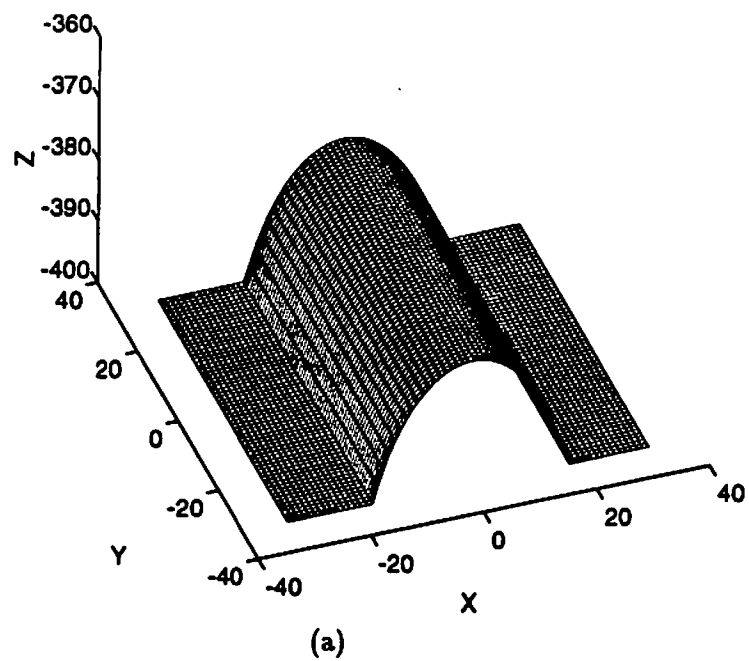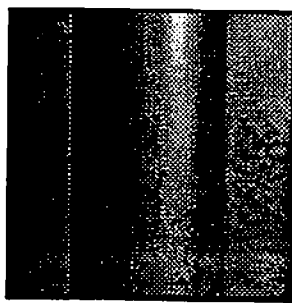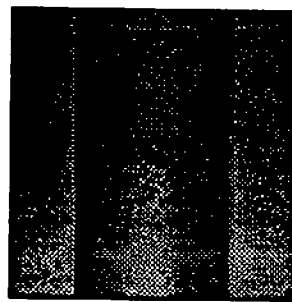
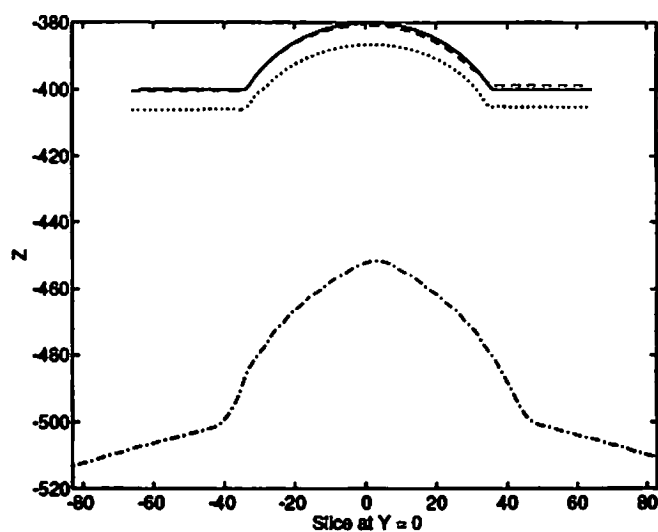Figure 7: Test Problem 3: (a) ground truth of a cylindrical surface, and (b)-(d) photometric stereo images.
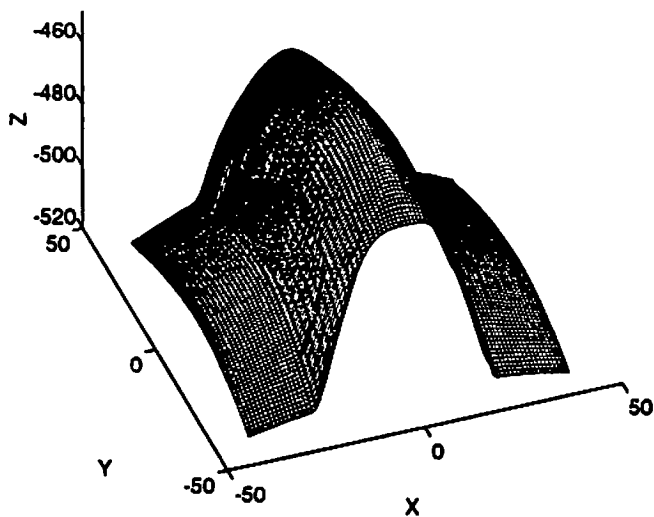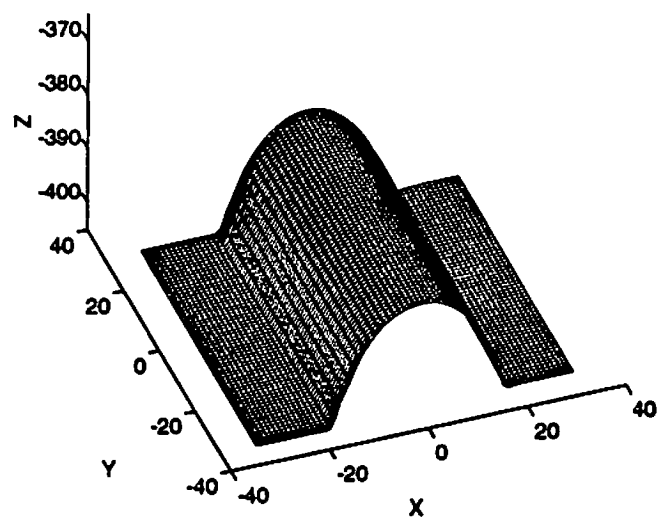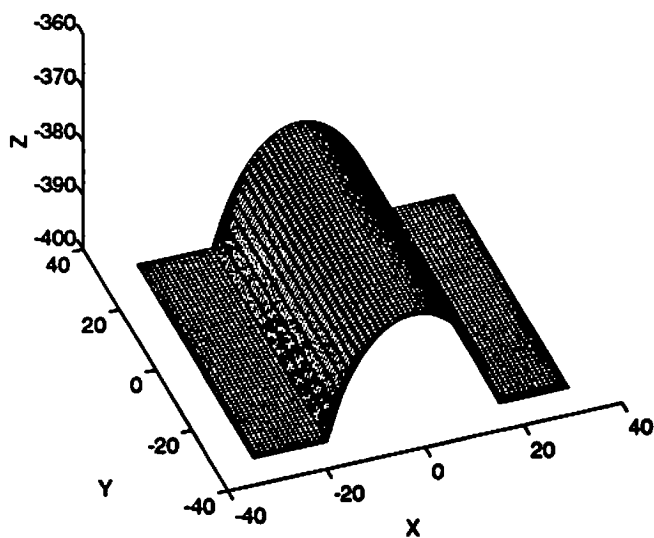
Figure 8: Reconstructed results of the cylindrical surface test problem with (a) a Lambertian model, (b) a general reflectance map, and (c) a general reflectance map model and a single depth constraint; and (d) their 1-D sliced plots.
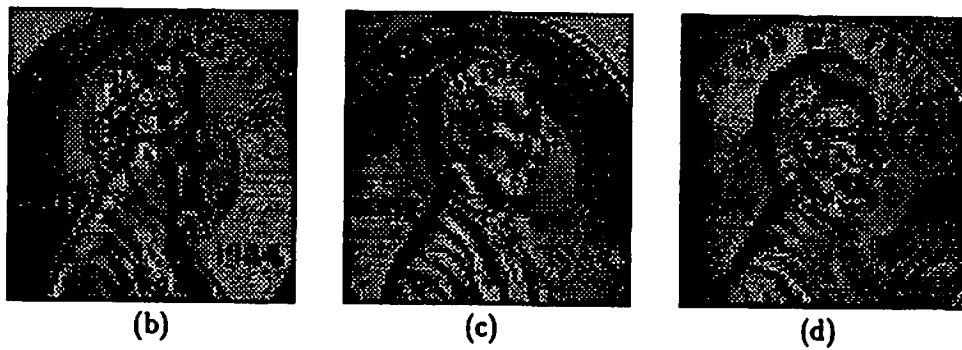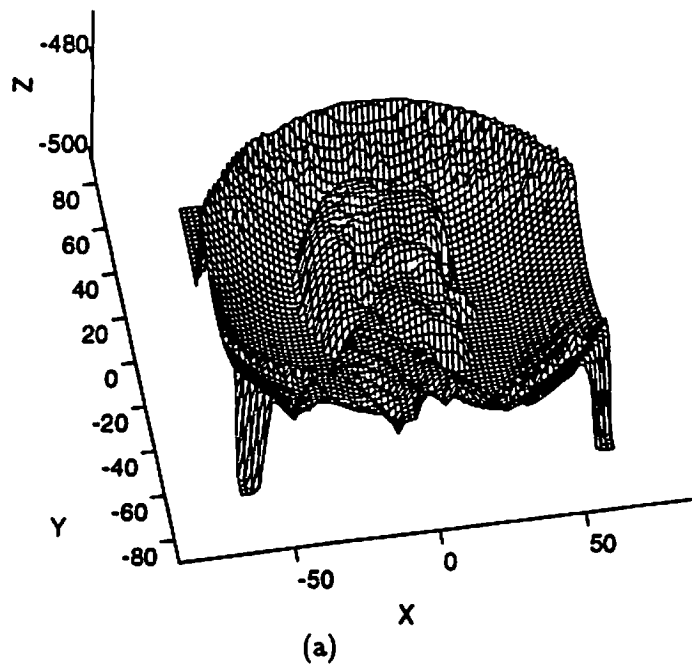
28

(a)

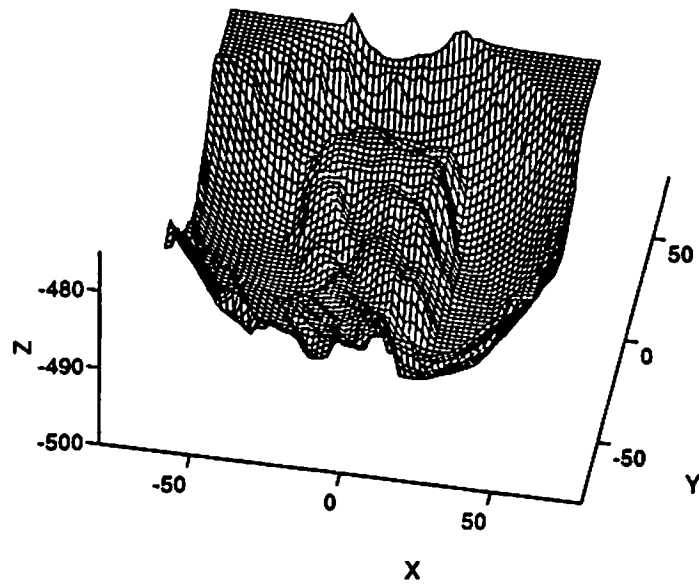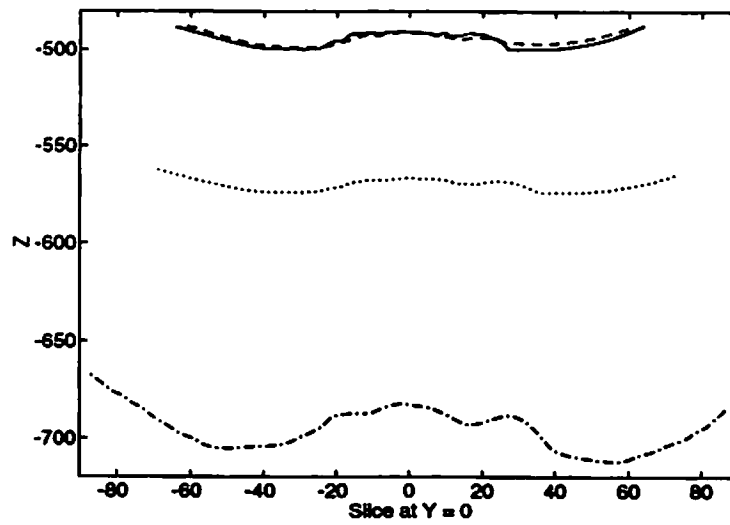(b)   (c)   (d)

Figure 9:   Test Problem 4: (a) ground truth of a penny surface; and (b)-(d) photometric stereo
images.

(a)

(b)

Figure 10: Results of the penny surface test problem: (a) reconstructed surface using a general reflectance map model with a single depth constraint; (b) 1-D sliced view of several reconstructed surfaces.